Full bandwidth electrophysiology of seizures and epileptiform activity enabled by flexible graphene micro-transistor depth neural probes

Andrea Bonaccini Calia[1], Eduard Masvidal-Codina[2,4], Trevor M. Smith[3], Nathan Schäfer[1], Daman Rathore[3], Elisa Rodríguez-Lucas[1], Xavi Illa[2,4], Jose M. De la Cruz[1], Elena Del Corro[1], Elisabet Prats-Alfonso[2,4], Damià Viana[1], Jessica Bousquet[1], Clement Hébert[1], Javier Martínez-Aguilar[2,4], Justin R. Sperling[1], Matthew Drummond[5], Arnab Halder[5], Abbie Dodd[5], Katharine Barr[5], Sinead Savage[5], Jordina Fornell[6], Jordi Sort[6,8], Christoph Guger[7], Rosa Villa[2,4], Kostas Kostarelos[1,5], Rob Wykes[3,5*], Anton Guimerà-Brunet[2,4*], and Jose A. Garrido[1,8*]

1 Catalan Institute of Nanoscience and Nanotechnology (ICN2), CSIC and The Barcelona Institute of Science and Technology (BIST), Campus UAB, Bellaterra, Barcelona, Spain.
2 Institut de Microelectrònica de Barcelona, IMB-CNM (CSIC), Esfera UAB, Bellaterra, Spain.
3 Department of Clinical and Experimental Epilepsy, Queen Square Institute of Neurology, University College London, London, United Kingdom.
4 Centro de Investigación Biomédica en Red en Bioingeniería, Biomateriales y Nanomedicina (CIBER-BBN), Madrid, Spain.
5 Nanomedicine Lab, National Graphene Institute and Faculty of Biology Medicine & Health, University of Manchester, United Kingdom
6 Departament de Fisica, Campus UAB, Universitat Autonoma de Barcelona, E-08193 Bellaterra, Barcelona, Spain
7 g.tec medical engineering GmbH, Guger Technologies OG, Austria
8 ICREA, Barcelona, Spain

* Corresponding authors: joseantonio.garrido@icn2.cat; r.wykes@ucl.ac.uk; anton.guimera@imb-cnm.csic.es

Mapping the entire frequency bandwidth of brain electrophysiological signals is of paramount importance for understanding physiological and pathological states. The ability to record simultaneously DC-shifts, infraslow oscillations (<0.1Hz), typical LFP signals (0.1-80 Hz) and higher frequencies (80-600 Hz) using the same recording site would particularly benefit preclinical epilepsy research and could provide clinical biomarkers for improved seizure onset zone delineation. However, commonly used metal microelectrode technology suffers from instabilities that hamper the high-fidelity of DC-coupled recordings, which are needed to access signals of very low frequency. Here, we use flexible graphene depth neural probes (gDNP), consisting of a linear array of graphene microtransistors, to concurrently record DC-shifts and high frequency neuronal activity in awake rodents. We show that gDNPs can reliably record and map with high spatial resolution seizures, pre-ictal DC-shifts and seizure associated spreading depolarizations together with higher frequencies through the cortical laminae to the hippocampus in a mouse model of chemically-induced seizures. Moreover, we demonstrate functionality of chronically implanted devices over 10 weeks by recording with high fidelity spontaneous spike-wave discharges and associated infraslow oscillations in a rat model of absence epilepsy. Altogether, our work highlights the suitability of this technology for *in vivo* electrophysiology research, and in particular epilepsy research, by allowing stable and chronic DC-coupled recordings.

Pathological electrophysiological signals resulting from epilepsy span over a wide frequency range, from fast activity, at hundreds of Hertz or higher, to less explored signals below 0.1 Hz, including DC-shifts (sustained over seconds to minutes) and infraslow oscillations [1,2,3]. In contrast to the widely-used AC-coupled recordings, DC-coupled recordings allow more comprehensive assessment of pathophysiological processes associated with either an increase in neuronal activity during seizures or a loss of neuronal activity during a spreading depolarization (SD)[4]. Clinically, electrophysiological biomarkers have been explored to guide surgical resection of the seizure-onset zone[5,6], however, improvement and refinements are still needed[7,8]. Indeed, intracranial clinical studies using large metallic electrodes suggest that the efficacy of current electrophysiological biomarkers could be improved by the inclusion of DC-shifts[9]. However, broad adoption of DC-shifts as a novel biomarker is limited by the poor capabilities of microelectrode technology to reliably record this type of electrophysiological signal *in vivo* with high spatiotemporal fidelity. This is due to polarization-induced drift and signal attenuation causing distortion of the measured signal by metallic electrodes[10,11,12]. Currently, the gold-standard for high-fidelity DC-coupled recordings is the glass micropipette; however, its use is limited to few-point measurements, hampering the spatial resolution required for seizure localization, and is not suitable for clinical applications. An alternative to commonly used passive electrodes are field-effect transistors (FETs), which are active transducers offering significant advantages in electrophysiology[13]. Among the few FET technologies that have been validated for *in vivo* electrophysiology, graphene-based FETs are particularly attractive because of the combination of material properties, including chemical and electrochemical inertness, high electrical mobility, biocompatibility, as well as a facile integration into flexible and ultrathin substrates[14]. Recent reports demonstrate the potential of graphene solution-gated field-effect transistors (gSGFETs) for neural interfacing[15,16]. A proof-of-concept of high fidelity DC-coupled recordings enabled by gSGFETs was demonstrated by mapping chemically-induced cortical spreading depolarisations (cortical-SDs) in anesthetized rats[17]. To explore its usefulness for epilepsy research, we have developed implantable flexible graphene depth neural probes (gDNP) capable of recording localised full bandwidth neuronal activity through

cortical columns and sub-cortical structures. We present a wafer-scale microtechnology process to fabricate ultra-thin gDNPs consisting of a linear array of graphene micro-transistors imbedded in a polymeric flexible substrate. In order to penetrate through the mouse cortex and reach the hippocampus without buckling, we adapted an insertion protocol that uses silk-fibroin (SF)[18,19] to temporary stiffen flexible gDNPs. The ability to detect electrophysiological biomarkers of epileptiform activity in preclinical rodent models of induced seizures and chronic epilepsy was validated experimentally[20]. These included seizure events such as spike-wave discharges (SWDs)[21] and high frequency oscillations (HFOs)[22,23]. Additionally, we highlight the suitability of graphene transistor technology to record concurrently fast and slow brain electrophysiological signals by benchmarking against a solution-filled glass micropipette recording, demonstrating the high-fidelity of the DC-coupled recordings obtained by the gDNPs. Here, we demonstrate the capability of gDNPs to record both active and passive ictal baseline shifts[24,25,26] as well as SD associated with seizure activity. Altogether, our results illustrate the potential of graphene micro-transistor technology to reveal mechanistic insights into the involvement of infraslow oscillations and DC-shifts associated with seizures *in vivo* in awake brain.

Results

Microfabrication, characterization and stiffening of the gDNPs. A graphene-based SGFET is a three terminal device in which single layer CVD graphene is used as the channel material in contact with the drain and the source terminals. Graphene is the sensing part of the device directly exposed to the neural tissue. The current in the graphene channel can be modulated or pinned by a third terminal given by a reference electrode (gate) which is also in contact with the conducting neural tissue (Fig. 1a). Thus, variations in the electrical potential in the tissue can be transduced into variations of the channel current; this transduction mechanism has been shown to offer a very versatile sensing platform for electrophysiology[27,28]. The flexible gDNP is a linear array of 14 recording transistors, each with an active area of 60x60 μm^2, and a pitch of 100 µm. The probe's tip design consists of a polyimide shank of 200 µm width and 1.6 mm length (Fig. 1b). A gDNP design with smaller SGFETs (20x20 μm^2) and narrower shank (150 µm width) has been also fabricated (Supplementary Fig. S1). gDNPs are fabricated on a 10 µm thick flexible polyimide (PI) substrate using a wafer-scale microfabrication process previously reported[16] (see Methods). A two-level metallization strategy, with metal levels interconnected using via-holes (Fig. 1b), reduces track resistance and improves sensor performance. To characterize gDNPs in saline solution we measure simultaneously the drain-source current (I_{DS}) versus the applied gate-source voltage (V_{GS}) for all the transistors on the shank with a fixed drain-source voltage (V_{DS}) using customized electronics (see Methods). gSGFETs exhibit very high transconductance (g_m) values due to a direct contact with the tissue, possible thanks to its biocompatibility and electrochemical inertness, and to the very high charge carrier mobility of graphene[29]. Fig. 1c shows the transfer curves as well as the normalized transconductance (g_m/V_{DS}), for all 14 gSGFETs of an exemplary gDNP device. The small dispersion of the charge neutrality point (CNP), defined as the value of V_{GS} where the I_{DS} reach its minimum, attests for the homogeneity of the gDNP. Furthermore, g_m shows a very stable response in a wide applied gate frequency range (up to 5 kHz), both in the hole regime, $V_{GS} < V_{CNP}$, and in the electron regime, $V_{GS} > V_{CNP}$ (Fig. 1d). Such constant frequency response is important for a proper calibration of the recorded signals[30]. The detection limit of the sensors is evaluated by means of the effective gate noise (V_{RMS}) integrated between 1 Hz and 2 kHz, with averaged values between 25-30 µV for all fabricated gDNPs (see Supplementary Fig. S2).

gDNPs are highly flexible, compared to traditional rigid depth electrodes, and although flexibility is advantageous once inserted into the tissue, this provides a challenge during insertion. To insert these probes we temporarily stiffen the gDNP using silk-fibroin (SF)[18,19]. The stiffening technique (see Methods) consists of a moulding process in which the gDNP is back-coated with SF, allowing the preparation of a rigid shank with a defined shape and thickness. We tuned the thickness of the SF by controlling the mould's trench depth, achieving two typical thicknesses of 80±10 µm and 150±12 µm (Fig. 1e). Mechanical assessment of the SF coated gDNP was performed using a buckling test, in which the perpendicularly positioned probes were driven against a flat and hard surface (Fig. 1f). An initial linear increase in force is observed for both coating thicknesses tested, while the probes remained straight before buckling (green box in Fig. 1f). Continued application of force results in buckling and bending (orange box in Fig. 1f), characterized by a peak in the force-displacement curve. The obtained peak forces, 101±21 mN for the 150 µm thick SF and 29±13 mN for 80 µm thick SF, are in good agreement with the previously reported values of peak forces of similar SF-coated neural probes[19,31]. We electrically characterized the gDNPs before and after the SF stiffening process, as well as before and after insertion and removal from an agarose gel brain model. Fig. 1g shows the distribution of the values of the normalized g_m as well as the effective gate noise (V_{RMS}) of all 14 transistors on a gDNP, confirming that neither the stiffening process nor the insertion in an agarose brain model impair gDNP performance in terms of transconductance or noise (Supplementary Fig. S3).

Fig. 1h depicts video frames of a SF-coated gDNP after insertion (insertion speed: 400 µm/s) in an agarose brain model; the images help to visualize the bending-free insertion of the gDNP shank and the fast water absorption (<10 s) of SF. Moreover, it can be seen that after removal from agar gel (180 s), SF is completely delaminated from the polymeric shank.

These observations confirm the suitability of the SF back-coating stiffening procedure to enable the flexible gDNPs reach target position in a brain-like tissue without bending; the fast dissolution of the shuttle once inserted enables the probe to quickly regain flexibility. This insertion strategy is only suitable for single-time use; for further insertions, the flexible gDNP needs to be recoated. We have assessed that the gDNP technology can withstand multiple coating and insertion procedures (Supplementary Fig. S4).

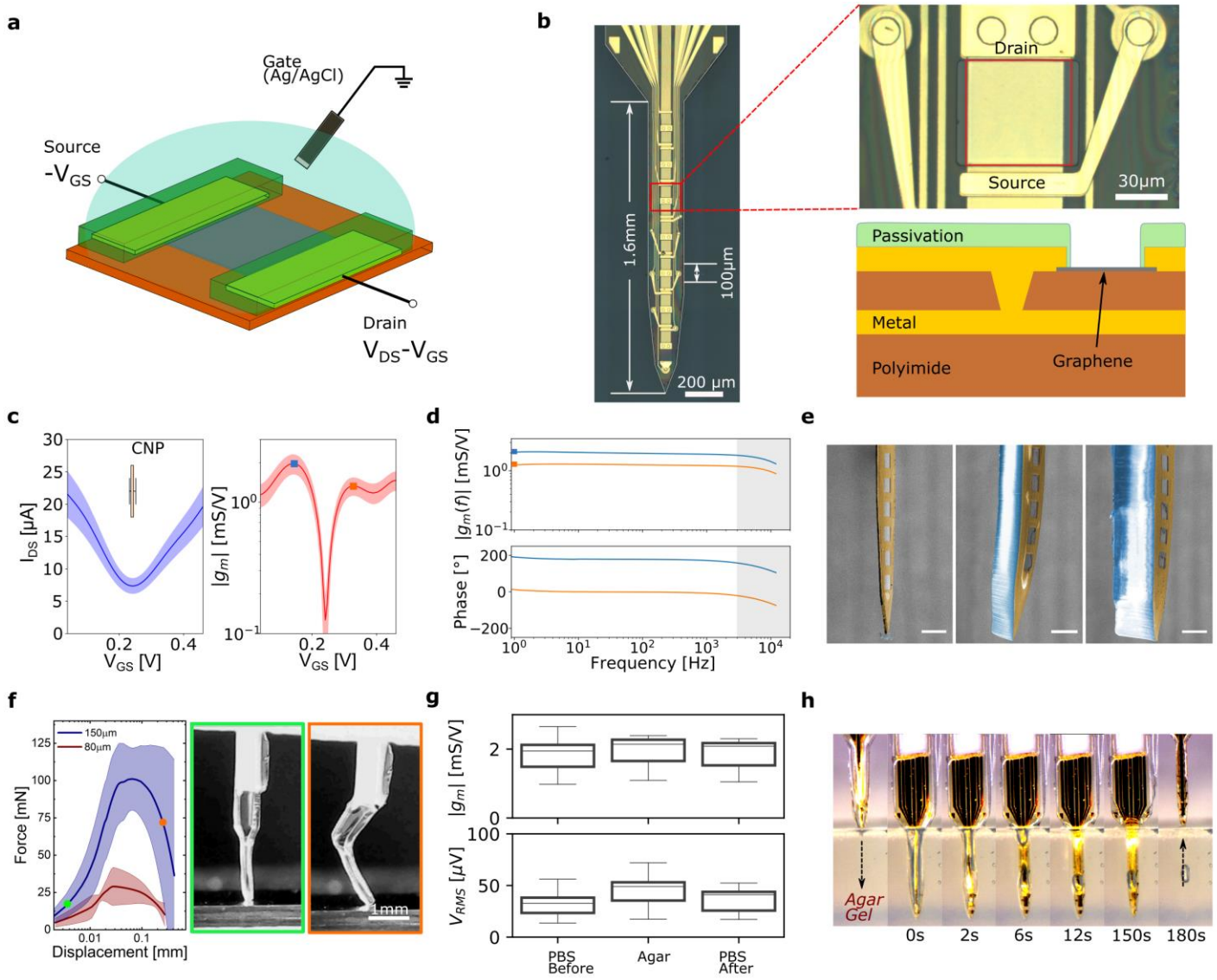

Fig. 1 Flexible graphene Depth Neural Probe (gDNP) technology and characterization. **a**, Schematic of a graphene solution-gated field-effect transistor (gSGFET) and biasing. V_{GS}: gate-source voltage, V_{DS}: drain-source voltage. **b** Optical microscope image of a gDNP containing 14 transistors with a pitch of 100 µm on a 200 µm wide polyimide shank. Right: blown up image of one gSGFET; the red contour highlights the graphene sensing area (60x60µm) of the transistor. The schematic of the cross section of one transistor shows the interconnected metal tracks strategy to reduce the shank width of the gDNP. **c-d**, Electrical characterisations of all 14 gSGFET on a gDNP in a 150 mM saline solution (V_{DS} = 50 mV). **c**, Mean values with standard deviation (shaded colours) of drain-source current (I_{ds}) and transconductance (g_m) versus V_{GS}. **d**, Transconductance spectroscopy of the gSGFET bias at the point of maximum g_m in the electron ($V_{GS} > V_{CNP}$, orange line) and hole regime ($V_{GS} < V_{CNP}$, blue line). Squares dots are the values of the g_m as measured in steady-state mode. The decay observed in the grey shaded areas is due to the filtering of the interfacing electronics. **e,** Coloured SEM images of the gDNP; uncoated (left), back coated with ~80 µm (middle) and with ~150 µm thick silk-fibroin (right); scale bar=100 µm. **f**, Mechanical assessment: averaged compression force vs displacement for the gDNP coated with two SF thicknesses (coloured areas are standard deviations, n=10 trials); the optical images correspond to two different conditions of the experiment. **g**, Functionality assessment after insertion in agar; the boxplot shows the distribution of the transconductance (g_m) values and V_{RMS} noise level for all gSGFETs on a gDNP measured in a PBS solution, inserted and measured inside an agarose gel brain model, and measured in the PBS solution after removal from the agarose gel. **h**, Image sequence of a SF-coated gDNP at different time points after insertion agarose gel brain model, revealing the timeframe of the degradation of the SF coating upon insertion.

Awake *in vivo* full bandwidth recording with gDNPs. We assessed full bandwidth recording capability by implanting a gDNP into awake, head-fixed mice. The electrophysiological signal measured by the graphene transistors was acquired with a customized electronic system that enables simultaneous recording in two frequency bands with different gains preventing amplifier saturation (Fig. 2a, Methods). gDNPs were implanted in the right hemisphere visual cortex (V1) and lowered until the tip reached hippocampal tissue. Baseline activity was recorded for (10-20 min). To induce network discharges and synchronicity of neuronal bursting 200nL of 4-AP (50mM), a selective blocker of Kv1 potassium channels[32,33] was focally injected into cortex adjacent to the gDNP (Fig. 2b).

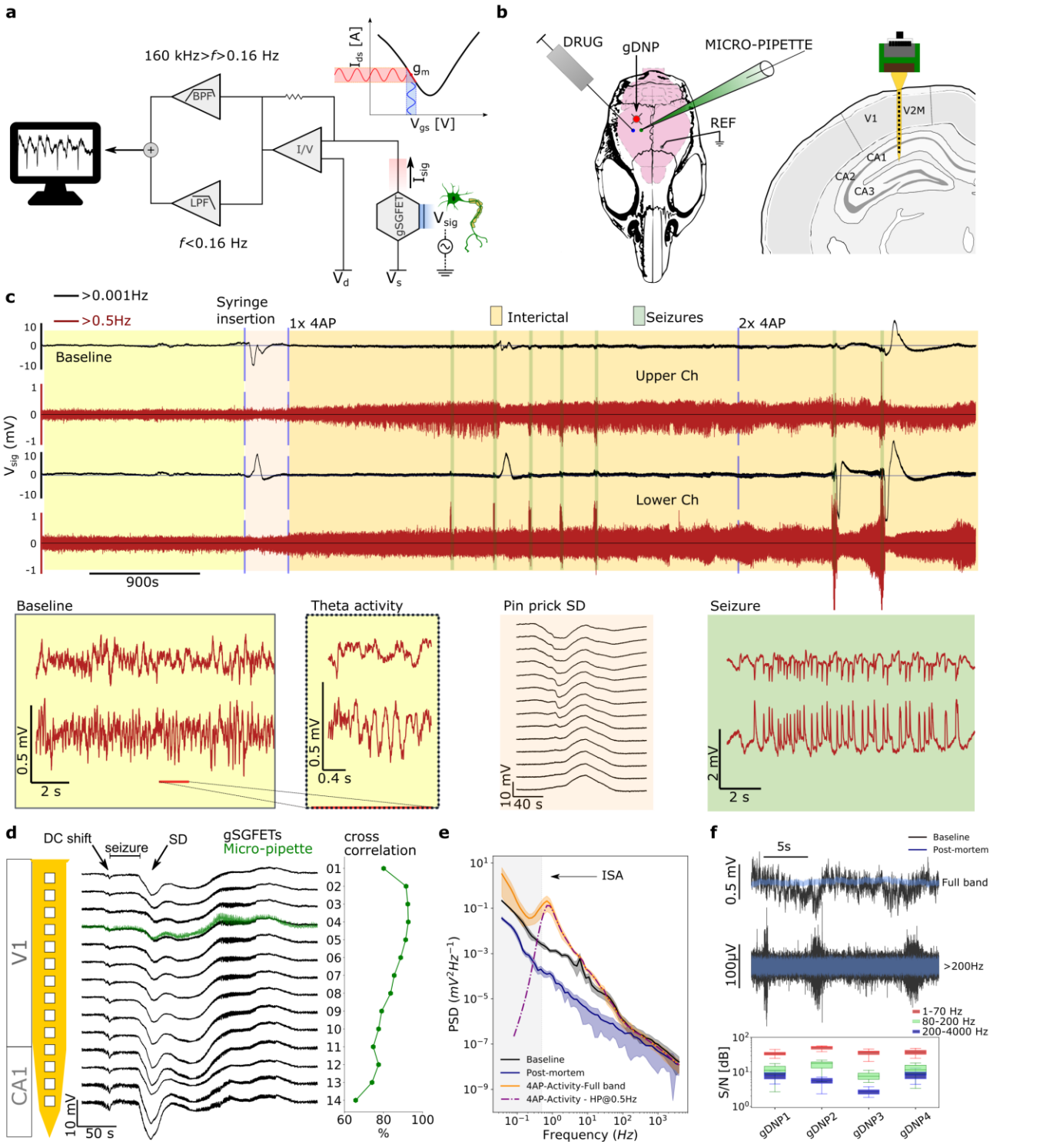

Fig. 2 Validation of *in vivo* full bandwidth recording capabilities of gDNPs. a, Schematic of the recording setup and concept of a graphene transistor as a transducer for neural recording. **b,** Schematic of a mouse skull with location on the brain of the gDNP, the glass micropipette and the needle to inject the chemoconvulsant drugs. Right, coronal view of the mouse brain with the localisation of the gDNP. **c**, Long electrophysiological recording (120 mins) of two channels on the gDNP array (top: visual cortex, bottom: hippocampus) showing the full bandwidth (f > 0.001 Hz, black) signal and the HP filtered signal >0.5 Hz (dark red). Baseline activity, pin-prick SD, increased neuronal activity after 4-AP injection and seizures, some of them followed by a SD. Below, different events in higher resolution: baseline (yellow) revealing theta activity in the lowest channel; profile visualization with recording from all 14 transistors following pinprick SD (beige); seizure activity shown for the uppermost and lowest channels of the gDNP (green). **d**, The recording shows the DC-shift concurring with seizure followed by a SD recorded by all 14 transistors (black). The superimposed green recording corresponds to the signal measured with the glass micropipette. The subfigure shows the low frequency cross-correlation (< 5 Hz), between the micropipette and all transistors on the shank. **e,** Averaged PSD over the electrophysiological recordings of all transistors during baseline, epileptiform activity, same activity HP filtered at 0.5 Hz (purple dashed-line) and post-mortem. The grey area highlights the low frequency part (<0.5 Hz) usually cut-off with conventional AC-coupled recordings. **f,** Comparison of a baseline activity (black) and a post-mortem (blue) in one channel of the gDNP (top: full band, bottom: HP>200 Hz). Lowest plot shows SNR evaluation for 4 *in vivo* experiments performed with 4 different gDNPs. The SNR is calculated for different bands (LFP:1-70 Hz, high frequency: 80-200 Hz and very high frequency: 200-4000 Hz; see Methods).

Full bandwidth recordings. Fig. 2c displays 2 hours of uninterrupted electrophysiological recording session (only the uppermost and the lowest channels of the implanted gDNP displayed); the complete data set is shown in Supplementary Fig. S5. The ability of the graphene transistors to have long and stable full-bandwidth recordings without the need for electronic off-set readjustments contrasts to the limitation of DC-coupled passive electrodes[34]. The black lines correspond to the full bandwidth signal (HP > 0.001 Hz) and the red lines to the signal high-pass filtered above 0.5 Hz (which is the expected signal recorded by AC-coupled electrodes)[35]. The coloured regions correspond to different experimental conditions during the recording: baseline, needle-induced pin-prick SD[36], interictal activity[5] induced by chemoconvulsant drugs, and seizures. During baseline recording in Fig. 2c, lower channels exhibit theta activity, correlated with animal movement, indicating that the gDNP reached the hippocampus, confirmed post-hoc by histological analysis of fixed brain sections (Supplementary Fig. S6). After injection of 4-AP epileptiform spiking evolved and five seizures (over 60 minutes) were elicited in this example, one of which was followed by a SD. A second cortical injection of 4-AP induced two additional seizures both followed by SDs that were detected first in the hippocampus. In 5 different mice injected with 4-AP, an average number of 7 ± 3 seizures were recorded in 60 min post drug injection. In this chemoconvulsant model SDs could be observed initially either in superficial cortical layers or the hippocampus (Fig. 2c and Supplementary Fig. S7).

The fidelity of DC-coupled recordings was validated by simultaneous recordings using a solution-filled glass micropipette. Fig. 2d shows the full bandwidth recording obtained with the gDNP (black lines) and the micropipette (green line) after injection of 4-AP. Both recordings reveal DC-shifts preceding the seizure and a SD occurring after the seizure. The DC-shifts measured by the gDNP have a similar shape, magnitude and temporal duration as the signal recorded by the glass micropipette. A cross-correlation analysis (signal filtered <5 Hz) of the signal recorded by the glass micropipette and the 14 gDNP transistors demonstrates a very high correlation (above 90%) for the channels located at the same cortical depth as the micropipette. The same high correlation is observed during hour-long recordings and for small, sudden DC-shifts (Fig. S23).

Assessment of the detection limits of gDNP. Post-mortem recordings were acquired to characterize the electrical noise level of the gDNP in the activity-free brain state and, consequently, to quantify the detection limit of the gDNP. Fig. 2e shows the averaged power spectral density (PSD) calculated using the recordings of all channels in a gDNP, obtained from different brain states (baseline, after injection of 4-AP, and post-mortem). Compared to the baseline PSD, the large amplitude of the PSD at low frequencies (< 1 Hz) after 4-AP injection is an indication of the interictal and DC-shifts in the brain. We have calculated the signal-to-noise ratio (SNR) in three different bands, 1-70Hz, 80-200Hz, and 200-4000 Hz (Fig. 2f). This analysis shows that the gDNPs are able to record electrophysiological signals in typical bandwidths with a SNR ratio higher than 1 dB.

Electrophysiological recording of characteristic epilepsy biomarkers. Epilepsy alterations of physiological brain activity include interictal spikes, fast activity at hundreds of Hz (such as HFOs) and pre-seizure active DC-shifts. We used two different pro-convulsive drugs (4-AP or picrotoxin, PTX) to induce and evaluate epileptic activity. Fig. 3a shows interictal activity and associated HFOs (>80 Hz) [22,23] recorded by three of the transistors of a gDNP, each located at a different depth in the mouse brain. Filtering between 80 – 600 Hz (red curves in Fig. 3a) reveals layer-specific bursting of HFOs and sharp wave ripples during interictal spikes with characteristic oscillations of 200-300 Hz and 400-600 Hz in the cortical and hippocampal channels, respectively[37] (Supplementary Fig. S8). Entrained interictal epileptiform activity was found in all channels before each seizure. Fig. 3b illustrates characteristic examples of sharp wave ripples and HFOs induced by 4-AP and by PTX recorded by the lowest channel of the gDNP (hippocampal CA1 region). The HFO and ripple traces shown in Fig. 3b exhibit high-frequency tones up to 600 Hz. The filtered traces (>200 Hz) are compared to the original traces (full-bandwidth) for verification of ripples. The advantage of the gDNPs to monitor concurrent DC-shifts and high-frequency activity is illustrated in Fig. 3c, which shows an epileptic spike-triggered SD, arising from the hippocampus. The layer-dependent silencing of the neural activity by the hippocampal SD is represented in Fig. 3d in terms of percentage of activity variation. The right plot in Fig. 3d shows the layer-dependent amplitude of the SD and the following hyperpolarization (more details of this analysis is provided in Methods and Supplementary Fig. S9), revealing that the silencing of the neural activity in the hippocampus is correlated with the amplitude and subsequent hyperpolarization wave of the SD. Silencing of neural activity in the hippocampus by the SD is visualized with more clarity in Fig. 3e, where the spectrograms for the upper and lowest channel are compared.

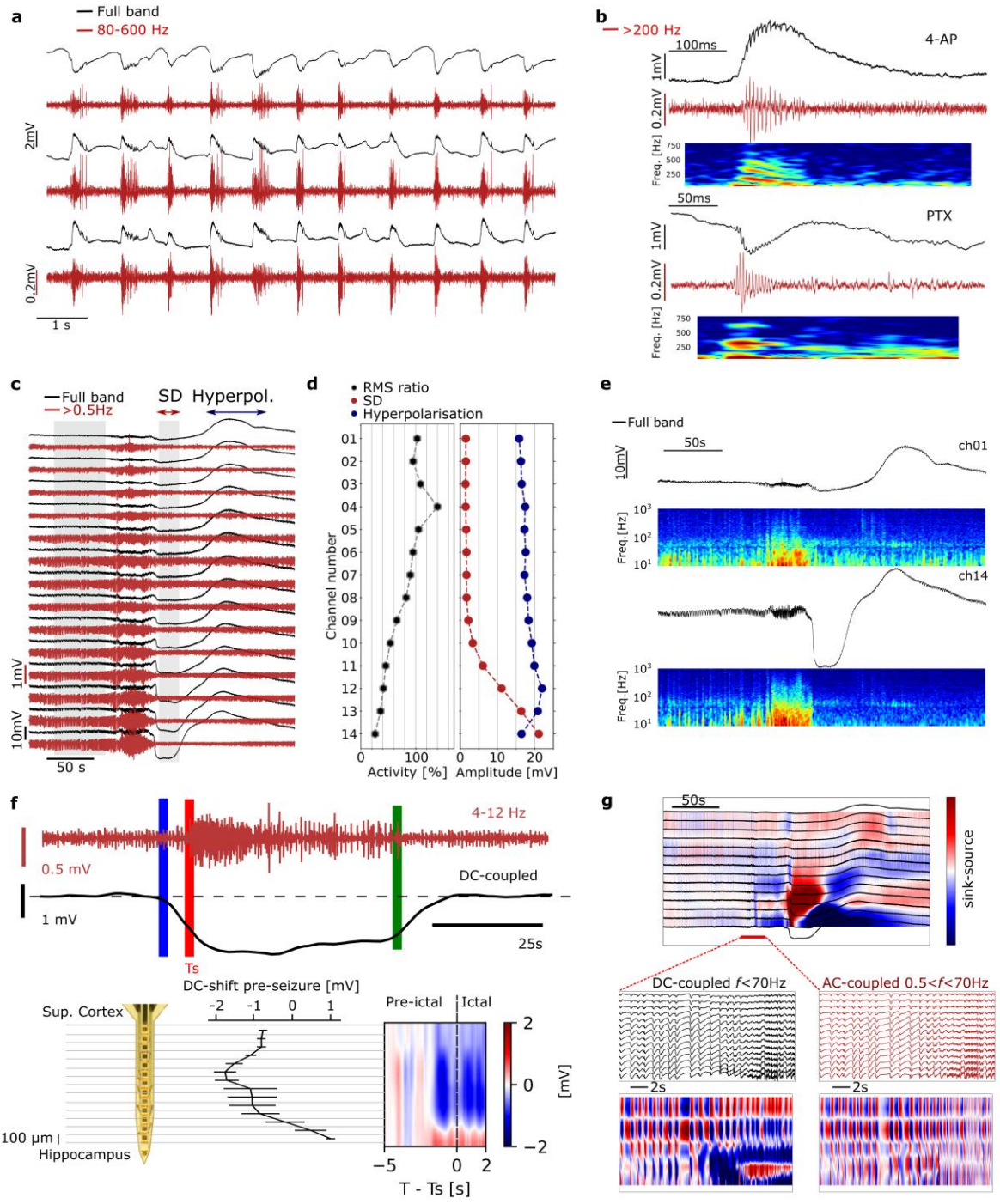

Fig. 3 Electrophysiological recording of characteristic epilepsy biomarkers. a, Interictal activity in three different channels of a gDNP (ch01, ch07, ch14) (red curves BPF 80 Hz – 600 Hz). **b**, Sharp-wave ripples and HFO recorded in the hippocampus induced by 4-AP and PTX (full band: black, HP>200 Hz: red); the figure also shows the corresponding spectrograms (range 10-800 Hz). **c,** Electrophysiological full band recordings (black curves) and HP filtered at 0.5 Hz (red curves) from the cortex (top channel) to hippocampus (bottom channel) illustrating a SD arising from the hippocampus after a seizure event. **d**, Left: percentage of neural activity variation calculated for each channel by comparing activity before and during SD (corresponding to the grey areas in (**c**)); Right: absolute amplitude of the SD and hyperpolarisation waves concurrent with the seizure. **e**, Hippocampal neural silencing during the SD illustrated by the spectrograms (range 10-1000 Hz) of the uppermost and lowest channels of the gDNP. **f**, DC-shifts precede seizures at the injection site after administration of 4-AP in awake mice. Top: Representative traces recorded by the gDNP showing a seizure event and the concurrent DC-shift after injection of 4-AP. Data is shown for two different bands: DC-coupled recording (<0.1Hz) and BP filtered (4-12Hz). Vertical coloured lines indicate the DC-shift onset (blue), the seizure onset (Ts, red) and seizure end (green). Bottom left: Depth profile of the peak DC-shift amplitude for each transistor (averaged over 4 seizures). The line represents the mean value of the DC-shift and bars the standard deviation. Right: Spatiotemporal dynamics of the DC-coupled voltage for the pre-ictal to seizure (ictal) transition (-5s to 2s). Data correspond to the average of 4 seizures in one mouse (Supplementary Fig. S10). **g,** Current-source density (CSD) analysis of the low frequency activity (< 70 Hz) corresponding to the recording shown in (c). Below: blow up of the pre-ictal to seizure transition (< 70 Hz), showing dipoles in the different layers of the cortex and hippocampus. The two graphs correspond to the CSD analysis performed with (left) and without (right) the contribution of the DC-coupled signal.

DC-shifts are typically associated with seizures[24,38] and can be differentiated into active shifts that precede the seizure, and passive shifts that follow the intense neuronal firing at seizure onset[39]. For these chemically-induced seizures events, we observed that the DC-shift preceded the seizure onset (Ts) by 2-3 s (n=4 seizures, Fig. 3f and Supplementary Fig. S10). Moreover, a layer dependent amplitude of the DC-shift is observed, with negative amplitudes in the cortical layers (close to the 4AP-injection site) and positive amplitudes recorded in the channels close to the hippocampus (Fig. 3f, bottom).The spatiotemporal dynamics of the DC-coupled extracellular potential for the pre-ictal to ictal transition is depicted in Fig. 3f (bottom right graph).
The inversion of DC-shifts can be used to identify current sources and sinks through the cortical laminae. Current-source density (CSD) analysis is a technique to identify source activation in a variety of focal neurological disorders including epilepsy[40,41]. CSD analysis (see Methods) of the data in Fig. 3c reveals a large net ionic sink in the hippocampal extracellular space after the seizure, followed by a large source at the beginning of the hyperpolarization wave (Fig. 3g). Enlarging the seizure onset region, 4 sink and source regions are identified through the laminae profile. CSD analysis computed with a high pass filtered signal (0.5Hz<f<70Hz) fails to report the ionic sinks preceding and during the seizure in the bottom layers (Fig. 3g, AC-coupled panel), illustrating the importance of using full-bandwidth recordings for CSD analysis to avoid misinterpretation of the CSD sinks and sources (Supplementary Fig. S11 illustrates additional examples of CSD analyses).

Chronic functional validation and biocompatibility assessment. We implanted gDNPs in the right-hemisphere somatosensory cortex of WAG-Rij rats (n=4), a rodent model of absence epilepsy[20], and obtained chronic full-bandwidth recordings over a 10-week period Fig. 4a. WAG-Rij rats exhibit frequent spontaneous spike-and-wave discharges (SWDs), a characteristic thalamocortical oscillation between 8-10 Hz[20] (see Methods). Implanted animals were connected 1-2 times per week for tethered recordings (using a commutator to enable free movement of the rats, see Fig. 4a and Supplementary Fig. S12).
Transistor curves were measured in each recording session to assess device stability, changes at the device/tissue interface and importantly, to permit selection of an optimal V_{GS} to maximise SNR; a feature possible with active sensor devices[28]. Fig. 4b shows the averaged transfer curves of a gDNP measured over 10 weeks (Supplementary Fig. S13). The stability of the transistors' performance is illustrated in Fig. 4c, which depicts the position of the CNP and the maximum value of g_m over the implantation period. The averaged g_m value remains approximately constant over the whole study. Since g_m is directly related to the tissue/graphene interfacial capacitance and to the carrier mobility in graphene, the g_m stability strongly suggests little or no variation of these two parameters. CNP (Fig. 4c) shows a significant shift (200 mV) during the few first days after implantation, which then remains stable for the rest of the experiment. We tentatively attribute the initial shift to the adsorption of negatively charged species, which reduce the intrinsic p-type doping of the graphene transistors[29].
Long-term functionality of the gDNP was assessed by evaluating the quality of the recorded signals over the implantation period using two parameters, normalized SWD power amplitude and the transistor noise (V_{RMS}). For further details, refer to Methods and Supplementary Fig. S13-Fig. S14. In Fig. 4d the variation of these two parameters over time is shown, demonstrating the ability of the implanted devices to monitor seizure activity with high fidelity during the whole implantation period. The slight increase in the normalized SWD activity could result from a strengthened coupling between neural tissue and the gDNP or from an increase in the seizure power and duration as the animal ages[42].
Correlation between SWDs and infraslow oscillations. The WAG Rij rat chronic model of absence epilepsy offers the possibility to investigate correlations between infraslow oscillations (ISO) and SWD events[43]. Thanks to the full-bandwidth capability of the gDNP, we were able to observe these correlations as well as a dipole across the neocortex upper and lower layers. Fig. 4e shows the uppermost and the lowest channel having opposite phase during each SWDs (Supplementary Fig. S15). The information contained in the DC-shift is lost after application of a HP-filter (>0.5 Hz), as typically used with conventional AC-coupled microelectrodes (Fig. 4e, grey). This observation persists over the implantation period as shown in Fig. 4f. To further evaluate the relation of ISO and SWDs, we calculated the phase of the signals (limited to the 0.01-0.1 Hz band) and the power of the neural activity associated to the SWDs (5-9 Hz). Fig. 4g displays the full-band and the ISO component (0.001-0.1Hz) of the signal recorded with one of the upper channels, together with the RMS of the SWD signal (5-9 Hz) and the ISO phase. Prior to the SWD events, whose onset is marked by the abrupt increase of the SWD RMS, the ISO phase is consistently observed to change (Supplementary Fig. S15 - Fig. S16). The correlation between the ISO phase and the SWD can be better illustrated by the joint probability distribution plot (Fig. 4g right panel) obtained from a long recording (1600s, >35 SWDs; see Methods). Fig. 4h depicts the correlation between ISO phase and the RMS of the SWDs for each channel, revealing an inversion in the lower layer of the neocortex (Supplementary Fig. S16). To further confirm the capability to observe these ISO preceding the seizure events, we calculated the depth profile of the DC-coupled signal (averaged for n=9 SWDs events) in a timeframe around the start of the SWDs. Preceding the SWD (with its characteristic positive DC-shift) by a couple of seconds, a small negative DC-shift was observed at superficial to medial layers (Supplementary Fig. S17).
This correlation between ISO and SWD was also observed in the other implanted WAG-Rij rats (n=4, Supplementary Fig. S18).

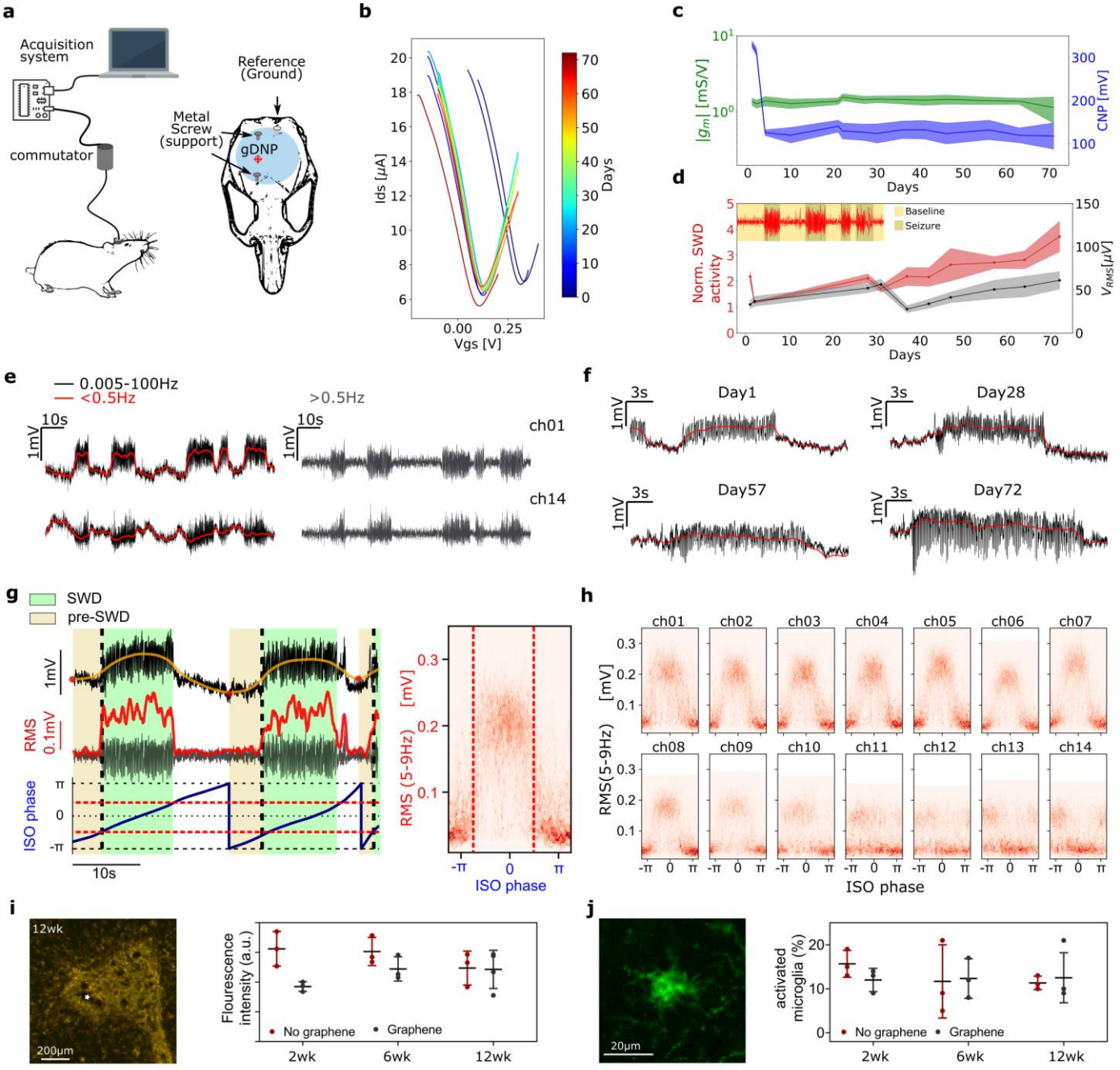

Fig. 4 Chronic assessment of stability, functionality and biocompatibility of gDNPs. a, Left: Cartoon of a WAG-Rij rat tethered via a commutator and the electronics for the data acquisition. Right: Schematic of the rat skull with the approximate location of the gDNP. **b,** Averaged transfer curves of all transistors of one gDNP over the implantation time. **c,** Averaged values of the maximum transconductance g_m (green) and the charge neutrality point (CNP, blue) of the transfer curves shown in (b). **d,** Normalized SWD activity over implantation time, calculated as the ratio of the SWD activity and baseline activity. Inset: example of SWDs events (red), highlighting the periods considered baseline and SWD. The graph also shows the average V_{RMS} noise (black) of all channels over the implantation period. **e,** SWD in the uppermost and lowest channels of the gDNP; DC contribution (red, <0.5 Hz) overlapped to the 0.005-100 Hz signal (black); in grey the same signal filtered above 0.5 Hz. **f,** Illustrative SWD events measured by the same channel at days 1, 28, 57, and 72. **g,** Amplitude-phase correlation between ISO and SWD. Top: recording from one of the transistors located in the rat cortex (ch02, black, 0.01-100Hz) showing two SWDs events (green shadow) concurrent with ISO (yellow, 0.01-0.1Hz) and the minimum of the ISO (red dot). Middle: RMS signal power of the SWD activity (red, 5-9Hz, evaluated with a sliding window of 0.5 s) overlapped with the HP filtered recording (grey, >1 Hz). Bottom, ISO phase (blue, 0.01-0.1 Hz evaluated with Hilbert transform); the red dotted lines marks the ISO phase region during a SWD. Right, joint probability density distribution of the ISO phase (x-axis) and the RMS of the SWD activity (y-axis) in the same channel for a long period of recording (1600s); colour indicates the probability density of the x-y pair, with white representing low density and red high density. **h**, Joint probability density distribution for all channels along the rat cortex (1600s). Results show a correlation between the ISO phase and SWD power with a phase inversion in deep cortical layers. **i-j,** Chronic biocompatibility assessment of SF-coated gDNPs implanted in Sprague-Dawley rats (n=20) by monitoring inflammatory markers. **i**, Fluorescent image of GFAP, as a measure of positive astrocyte cells, in the area of insertion, at 12 weeks post implantation (the white star shows the insertion point). Time evolution (2, 6, 12 weeks) of the fluorescence intensity (calculated at 150μm from the probe sites) obtained for flexible probes with graphene (grey), and probes without graphene (red). **j,** Example of microglial activation (fluorescence image). Time evolution (2, 6, 12 weeks) of activated microglia in the vicinity of the implanted probes (in an area of 0.7 mm^2) obtained for the two types of probes (graphene, no-graphene).

Chronic biocompatibility of implanted gDNP. We also conducted an extensive chronic biocompatibility study to assess any potential neuro-inflammation caused by the invasive nature of the penetrating neural probes, the presence of CVD graphene, or by the release of SF following implantation. Neural probes with or without graphene at the recording sites were implanted in adult, male Sprague-Dawley rats (n=20). Histological and immunohistochemical studies were conducted at 2, 6, and 12 weeks' post-implantation and compared to the contralateral hemisphere, without device implantation (Methods and Supplementary Fig. S19 - Fig. S20). An additional small cohort of animals (n=3) were implanted with commercially available rigid depth neural probes with similar dimensions (NeuroNexus, Supplementary Fig. S19). Fig. 4i shows a fluorescence image of GFAP immunostaining (positive marker for astrocyte cells) in the area of insertion 12 weeks post implantation (brain sections at 800 μm from pia). There was no significant difference in the number and morphology phenotype of astrocyte cells (typically associated with inflammation) in the area directly surrounding the implanted probe site, or on comparison between probes with or without graphene (Fig. 4i, right graph). No significant difference was observed at 2, 6, and 12 weeks' post-implantation, and values are in the same range as in the contralateral hemisphere where no probe was inserted (Supplementary Fig. S19). The activation state of microglia, assessed by morphological analysis of cells stained for ionized calcium binding adaptor molecule 1 (Iba-1), showed no significant increase in the abundance of activated microglia present in the area surrounding the implantation site (Fig. 4j). Additional immunohistochemical analysis showed no sign of an inflammatory response over the 12-week period for either device used, comparable with commercially available rigid probes (Supplementary Fig. S19). Recently published biocompatibility data from some of our laboratories using flexible gFET devices designed with large graphene surface areas implanted epicortically, also showed no significant adverse tissue response chronically[44]. Altogether, the chronic biocompatibility study here indicated that gDNPs are suitable for deep brain structure chronic implantations, inducing no significant tissue damage nor neuroinflammatory responses.

Outlook

In this work, we demonstrate the capability of gDNPs based on linear arrays of gSGFETs to record electrophysiological brain activity in a wide temporal range, with fidelity similar to solution-filled glass micropipettes but with superior spatial sampling. gDNP is a novel technology that allows concurrent recordings of DC-shifts, ISO and high frequency oscillations in preclinical epileptic models through the cortex laminae to upper hippocampal layers.

Together with validation of the chronic functionality of implanted gDNPs and their biocompatibility, our work underlines the very distinct advantages of this technology for *in vivo* epilepsy research. In particular, gDNPs allowed us to reveal in rodent models of drug-induced seizures and chronic epilepsy[20] associations between DC-shifts (including ictal baseline shifts and spreading depolarizations [24,25,26,45,46]) and higher frequency activity (including SWDs[21] and HFOs[22,23]).

The reliability, stability and high fidelity of the recordings presented in this work suggest that this technology could be eventually used to record clinically relevant electrophysiological biomarkers. In this respect, we envision that clinical development of this technology could be directed towards neural probes capable of simultaneous high-quality wide-band (DC to HFO) recordings from multiple brain regions during pre-surgical monitoring. Moreover, this technology could be applied combining depth and subdural gSGFET arrays capable of stable DC-coupled recordings with high spatial resolution, which will offer advantages over current technologies for epilepsy and neurocritical care[47]. In particular, it is expected that this technology can help improve identification of seizure onset zones (SOZ) and ultimately surgical outcome[5]. Currently, long-term seizure freedom after surgery is only around ~50%[48]; thus, improvements in a technology that more precisely defines surgical margins is warranted. The few studies which have investigated DC-shifts report that these signals co-localise with seizure onset zones, and are more spatially restricted than conventional EEG recordings[49]. Therefore, routine inclusion of accurate DC-coupled recordings to surgical monitoring, that can be enabled by the technology described in this work, could result in less extensive, yet more effective surgical resections[9]. Beyond its use for epilepsy research, we envision that this technology can be applied to advance our understanding of other neurological diseases associated with SD, including traumatic brain injury, stroke and migraine[50].

Methods

Graphene growth, transfer and characterization. Graphene was grown by chemical vapor deposition (CVD) on copper foil (Alfa Aesar Coated). Prior to growth, copper foil was electropolished for 5 min in a H_2O (1 L) + H_3PO_4 (0.5 L) + ethanol (0.5 L) + isopropanol (0.1 L) and urea (10 g) solution[51]. The CVD reactor consists of a tubular three zone oven with a quartz tube (1600x60 mm). After loading Cu foil, an annealing step (1h) was performed, prior to growth, at 1015ºC under a 400 sccm Argon flow at 100 mbar. This was followed by the growth step (15 min growth step), at 12 mbar under a gas mix of 1000 sccm Argon, 200 sccm hydrogen, and 2 sccm methane. Transfer of the graphene from copper foil to polyimide was achieved using a wet-etching chemical method. A supporting poly(methyl methacrylate) PMMA 950K A4 was spin-coated on the graphene/copper foil and left to dry for 12 h. Back side graphene is removed with a 10% HNO_3 solution. Subsequently, the sample was laid on the etchant solution composed of $FeCl_3$/ HCl (0.5M/2M) to remove copper for at least 6 h. Next the graphene/PMMA stack was rinsed in DI water multiple times before transfer onto the polyimide-coated wafer. The wafer was dried for 30 min at 40 ºC on a hot plate, and annealed in a vacuum hotplate

by increasing the temperature gradually up to 180 ºC. Finally, the PMMA was removed in acetone and isopropanol. CVD-grown graphene was characterized by Raman spectroscopy using a Witec spectrograph equipped with a 488 nm laser excitation line. To assess the quality of the graphene film (see Supplementary Fig. S21) Raman maps of 30 x 30 μm^2 (with 1 μm resolution) were acquired using a 50x objective and the 600 g nm^{-1} grating and laser power of 1.5mW.

Microfabrication of flexible gDNPs. Flexible neural probes were fabricated using standard microelectronic fabrication technology on a rigid 4-inch sacrificial Si/SiO2 wafer. A 10 μm thick polyimide (PI-2611, HD MicroSystems) layer was spin-coated and cured at 350 °C in a N2 atmosphere. To reduce the shank width of the depth neural probes, we used a two-metal level strategy in which the metal tracks, separated by PI, are interconnected by via-holes. After evaporation and definition (via lift-off) of a first metal layer of Ti/Au (10/100 nm), a 3 μm-thick PI layer was spin-coated and cured. A protective mask of Al (200nm) was used to etch the second PI layer by oxygen plasma and form the via-holes. On top of the via-holes a second metal layer of Ti/Au (10/100 nm) was applied to interconnect the two metal layers. CVD graphene was transferred onto the patterned wafer as described in the section above. After removing the PMMA protection layer, the graphene active areas were defined by means of an oxygen-based reactive ion etching. A sandwich-like contact strategy was used to improve the contact at the drain and source terminals; the used top metal structure was Ni/Au (20/200nm). For passivation, a 2μm-thick chemically resistant polymer is deposited (SU8-2005 MicroChem) with open windows in the channel region. Finally, the gDNP structure was defined in a deep reactive ion etching process using the thick AZ9260 positive photoresist (Clariant) as an etching mask. The polyimide probes were then released from the SiO2 wafer and placed in a zero insertion force connector in order to interface our custom electronics. A way to further improve the transconductance of the flexible gSGEFTs can be achieved by adding an ultra-violet ozone (UVO) cleaning of the contact region at the graphene/metal interface, as recently demonstrated for flexible graphene neural sensors[52].

Characterization of gDNPs in saline. The graphene SGFETs on the neural probes were characterized in PBS solution (150mM). Drain to source currents (Ids) were measured varying the gate–source voltage (Vgs), versus a Ag/AgCl reference electrode which was set to ground. Steady state was ensured by acquiring the current only after its time derivative was below a threshold (10^{-7} A s^{-1}). The detection limit of the graphene SGFET were assessed by measuring the power spectral density of the DC current at each polarization point V_{GS}. Integrating the PSD over the frequencies of interest (1Hz-2kHz) and using the transconductance allowed us to calculate the root-mean-square gate voltage noise V_{RMS}. The noise measurement was performed in a Faraday cage, with DC-batteries powering the amplifiers, in order to reduce any 50 Hz coupling or pick-up noise. Additionally, the frequency response of the device's transconductance was measured by applying a sum of sinusoidal signals at the electrolyte solution through the reference electrode and by measuring the modulation of the drain current. The acquired signals were split into two bands, low frequencies (≈ 0–10 Hz), at which drain–source current was simultaneously acquired for all transistors in an array, and higher frequencies (10 Hz–30 kHz), at which each transistor was recorded individually.

Back coating of gDNP with silk fibroin. Compared to other natural biopolymers, silk fibroin offers excellent mechanical properties, extremely good biocompatibility, biodegradability, and the versatility of structural readjustments[53,54,55]. Further, the byproducts of the SF degradation by enzymes (e.g. proteases) have low antigenicity and non-inflammatory characteristics[56,57]. Temporary stiffening of the gDNPs with silk fibroin is achieved using a micro-structured PDMS mould with the shape of the neural probes. To fabricate the moulds, PDMS is cast on a standard 4-inch silicon wafer with pre-patterned 100 μm and 200 μm thick SU8 (SU8-2050) epoxy resin. The back-coating procedure is as follows: first, the probe is placed in the mould trench filled previously with water, with the transistor side facing down. Through surface tension the probe self-aligns in the mould. After evaporation of the water, silk fibroin (Sigma Aldrich, Silk, Fibroin Solution 50 mg/mL) was applied via a syringe to the mould's trench. We double coat the shank in drying intervals of 20 minutes and then slowly increase the temperature on a hotplate to 80 °C, leaving the SF curing for 1h 30 minutes. By increasing the duration of the water annealing step we managed to have a delayed dissolution time compared to SF cured at room temperature. After curing, the coated probe can be easily removed from the PDMS mould (Supplementary Fig. S3). In all presented *in vivo* experiments we implanted the flexible gDNPs with a 150 μm thick SF back-coating.

Assessment of mechanical properties of the stiffened gDNPs. Standard compression tests against a hard silicon (Si) substrate were performed to assess the mechanical properties of our SF-coated probes. Buckling experiments were carried out in a UMIS nanoindenter from Fischer-Cripps Laboratories. A custom clamp was fabricated to fix the probes at the end of the indenter shaft that, in turn, was connected to the actuator and load cell. Buckling tests were carried out at a loading rate of 8.8 mN/s. Once the indenter detected noticeable buckling the test was automatically stopped. The maximum applied load that the indenter can apply is 500 mN. Applied force vs displacement was measured until the probe started buckling and eventually broke down. We additionally measured the Young's modulus of the SF cured at 80 ºC by means of nano-indentation tests. SF was drop casted on a 2x2cm^2 Si chip and cured. The indentation measurements were performed using a NHT2 Nanoindentation Tester from Anton-Paar equipped with a Berkovich pyramidal-shaped diamond tip. A maximum applied load of 5 mN was applied with a loading segment of 30 s followed by a load holding segment of 10 s and an unloading segment of 30 s. The hardness and reduced Young's modulus are reported as an average value of at least twenty indentations, performed on top of each sample (in the central region). Young's modulus values in the range of 10 GPa where measured for 80 ºC cured SF (see Supplementary Fig. S22).

Electronics for in vivo recordings with gDNPs. The experimental setup used to perform the *in vivo* recordings provides Vs and Vd bias control and current-to-voltage conversion for up to 16 channels (g.RAPHENE, g.tec medical engineering GmbH, Austria). The instrumentation splits the recorded signals into two bands with different gains: low-pass filtered (LPF, < 0.16 Hz, 10^4 gain) and band-pass filtered (BPF, 0.16 Hz < f < 160 kHz, 10^6 gain). Two custom Simulink models were used: i) to perform the transfer curve of the microtransistors once inserted and at the end of the experiment; ii) to set the Vs and Vd bias and acquire the recorded signals. Signals were sampled at 9.6 kHz and at 19kHz depending on the type of experiment (Supplementary Table1).

Ethical approval and animal handling for acute and chronic experiments. Animal experiments were conducted in accordance with the United Kingdom Animal (Scientific Procedures) Act 1986, and approved by the Home Office (license PPL70-13691). C57BL/ mice were bred (2-4 month old males), while WAG rats were imported (Charles river, used 6-9 months of age). Animals were housed on 12 h/12 h dark/light cycle, and food and water were given *ad libitum*. Prior to headbar sugery, animals were group housed, but after this, animals were individually housed.

Acute preparation surgeries for headbar attachment and craniotomy. For both surgeries, aseptic techniques were used with mice anaesthetized using isoflurane (988-3245, Henry Schein, U.S.A.) and placed in a stereotaxic frame (David Kopf Instruments Ltd., U.S.A.). Viscotears applied (Bausch + Lomb, U.S.A.) and pain relief, which consisted of sub-cutaneous Bupenorphine (0.5 mg / Kg;Ceva, France) and Metacam (15 mg /Kg; Boehringer Ingelheim, Germany), were injected. Saline was administered just before recovery or every 45 mins depending on the length of surgery. To apply the headbars for the Neurotar system the skin on the top of the head was cut to expose the skull. The skull was cleaned and dried, which enabled drilling (RA1 008, Henry Schein, U.S.A.) of a small hole in the left hand visual cortex for a metal support screw (00-96X3-32, Plastics One, U.S.A.). Using vetbond (1469SB, 3M, U.S.A.), the headplate (Model 9, Neurotar, Finland) was firmly attached and strengthened using dental cement before Kwik-cast (KWIK-CAST, W.P.I., U.K.) covered the exposed skull. Mice were checked daily to ensure recovery. After at least 5-days of recovery, habituation was performed by placing the mouse in the Neurotar frame for increasing periods of time (15-60 mins) over several days. On the day of recording, a craniotomy was performed. Under Isoflurane anaesthesia, with administration of pain medication and intra-muscular Dexamethasone (1 mg / Kg; intra-muscular; 7247104; MSD Animal Health, U.S.A.), two areas were exposed. A large (2x2mm) craniotomy over somatosensory and visual cortex on the right-hand side and a small drill hole over the motor cortex on the left hand side. Cold Cortex buffered saline was continually applied to the craniotomies. After completion, exposed dura was covered with Cortex buffered saline, sterilised slygard (~200 μm thickness), and a kwik-cast layer. After ~2-hours post-recovery, the animal was moved to the Neurotar frame and the craniotomies were exposed by removal of the kwickcast and sylguard. The gDNP was carefully connected to a PCB and lowered using a micromanipulator to just above the dura over the visual cortex. The dura was gently pierced using either micro-dissection scissors or a 26-gauge needle and gDNP lowered ~2 mm into the brain. A reference wire ($Ag/AgCl_2$) was placed in the ipsilateral motor cortex and g.tec hardware (see *Electronics for in vivo recordings with gDNPs*) used to perform the transfer curve to determine the optimal V_{GS} and initiate recordings (Supplementary Fig. S4). Chemoconvulsant was injected into the brain using a Nanofil injection system (W.P.I., U.K.). At the end of the experiment, sodium pentobarbital was administered intra-peritoneally.

Recording with solution-filled glass micropipette. Borosilicate capillary tubes (OD: 1.50mm, ID: 0.86mm, Warner Instruments) were pulled using a horizontal puller (Sutter instruments P-97, resistance of 3-5 MOhm) and filled with artificial Cerebral Spinal Fluid (NaCl: 119mM, KCl: 2.5mM, CaCl2: 2.5mM, MgSO4: 1.3mM, NaH2PO4: 1.25mM, NaHCO3: 25mM, Glucose: 10mM) and attached to an Axon instruments CV-7B head stage. A micro-manipulator (MM3301, WPI) was used to position the pipette above the cortical surface before insertion approximately 400μm into the cortex. The head-stage was provided with the same reference as the gDNP, a chlorinated silver wire touching the ipsilateral motor cortex. The headstage was connected to a Multiclamp 700B amplifier (Axon Instruments) operating in current clamp mode. Analogue-Digital Conversion and TTL pulse delivery for temporal synchronisation was achieved using the Micro1401 MkII (CED, Cambridge, U.K.). Data was acquired using WINEDR sampling at 20 kHz with a 4 kHz Bessel filter.

Chronic preparation surgery and recording. First, the gDNP was fibroin coated, as described above, to aid insertion. The rat was anaesthetised to a surgical depth using Isoflurane. After placement in a stereotaxic frame, Viscotears were applied and pain medication, which consisted of Bupenorphine (0.15 mg / Kg; sub-cutaneous; Ceva, France) and Metacam (4.5 mg /Kg; sub-cutaneous; Boehringer Ingelheim, Germany), was applied. The skull was cleaned and dried. Small burr holes (~1 mm) were drilled at four positions: 1) Somatosensory cortex for gDNP (since the perioral somatosensory cortex is the focal area for SWDs [58]) ; 2) contralateral cerebellum for a reference Ag/AgCl wire held in place by a nylon screw; 3) Motor cortex, ipsilateral, for a support screw ; and 4) Visual cortex, ipsilateral, for a support screw. The metal screws were inserted and provided structural support for the dental cement. Next, the gDNP and the reference wire were inserted, and a DC characterisation curve confirmed that the transistors were performing optimally. Dental cement, mixed with vetbond, was applied around the PCB for support. Animals were weighed daily and their physiology was monitored to ensure a full recovery. For recording, animals were anaesthesia-free and moving, with the PCB-interface on the head connected to an Omnetics cable (A79635, Omnetics, U.S.A.) that interfaced with the g.tec recording hardware as described above. After ~5-minutes for settling, a DC characterisation curve was recorded to allow accurate calibration of the gSGFETs. A script calculated the optimal V_{GS} based on the transfer curves. Recordings were performed for ~10-60 minutes twice a week for 10 weeks. After recording, the Omnetics wire was disconnected and a protective cap was applied.

WAG/Rij Strain of rats

WAG-Rij rats were used as a model of absence epilepsy. Spike-wave activity in cortical EEG of adult WAG/Rij rats have a frequency of 7-10Hz and can last from just a few, to up to 40 seconds in duration. From an age of 6 months WAG/Rij rats display several hundred spike wave discharges (SWDs) a day[20]. In addition to electrophysiological signs, mild behavioural phenotypes concurrent with SWD similar to human absence epilepsy are displayed. These include facial myoclonic jerks, twitching, accelerated breathing, head tilting and eye blinking. Drugs prescribed for human absence epilepsy suppress SWDs in WAG/Rij rats, and these rats have been used to predict the action of antiepileptic medication and other experimental treatments[59].

Data analysis. All electrophysiological data were analysed using Python 3.7 packages (Matplotlib, Numpy, Neo and Elephant) and the custom library PhyREC (https://github.com/aguimera/PhyREC). The conversion of the recorded current signals (LPF and BPF) to a voltage signal was performed by summation of the two signals and inverse interpolation in the in vivo/chronic measured transfer curve of the corresponding gSGFET[17]. Even for large signals (tens of mV), this calibration method yields distortion-free signals in contrast to using a fixed transconductance value[30]. The transfer curves were always measured at the beginning and end of every recording to ensure that no significant variations were present and to detect any malfunctioning transistor. Moreover, all recordings presented in the manuscript have been calibrated with the nearest-recorded transfer curve to ensure high fidelity in the voltage-converted signals.

In order to assess the detection limit in the conventional frequency bands (>1 Hz), the recordings (Fig 2f) of the baseline were directly compared with post-mortem recordings. For instance, applying a digital filter (> 200 Hz) and comparing post-mortem with baseline validates the ability of gDNP to record spontaneous high-frequency activity (> 200 Hz) arising from groups of neurons in a non-pathological brain state (upper plot in Fig 2f). Beyond this qualitative comparison, the SNR shown in Fig. 2f was evaluated by the ratio of the RMS mean value over 25s of recording of baseline (spontaneous activity) and post-mortem (no activity). The signal is BP filtered in three different bands corresponding to the LFP activity (1-70 Hz), high frequency (80-200 Hz) and very high frequency activity (200-4000 Hz). RMS values were calculated with a sliding window of 500ms for the 1-70 Hz band and with a sliding window of 10ms for the other two bands. The whisker plots (boxplots) where created with a Python library (seaborn.boxplot) to show the data distribution for working transistors on the gDNP (gDNP1= 10; gDNP2=12, gDNP3= 12, gDNP4=14); The line in the box correspond to the median value, the box shows the quartiles of the dataset while the whiskers extend to show the maximum and minimum values. SNR for the different bands is evaluated from a total of 4 in-vivo experiments with 4 different gDNPs (Fig. 2f). SNR is expressed in dB ($20*\ln(RMS(S)/RMS(N))$; S is the "signal" during the baseline recording, N is the "noise" measured during the post-mortem recording. The silencing of neuronal activity shown in Fig. 3d, was extracted using the AC-coupled recording (HP >0.5 Hz). Then the RMS values of the pre-ictal phase (calculated with a sliding window of 1s) are averaged over 50s time. Similar analysis was performed for the time during the SD (15s, shaded areas in Fig. 3d). The ratio of the two averaged RMS values corresponds to the neuronal activity variation [%] (before and during the SD). The amplitude of the hippocampal SD and hyperpolarization wave in Fig. 3d, is evaluated using the recording LP filtered in the infra-slow regime (<0.5 Hz) and re-sampled at 3 Hz (instead of 9.6 kHz used in the original recording). The zero of the voltage was set using the mean value of the signal 50s before the pre-ictal phase (Supplementary Fig. S9), the minimum and maximum values for each channel were extracted (corresponding to the SD and the hyperpolarisation amplitude respectively).

For the analysis of the DC-shifts pre-seizure (Fig. 3f and Supplementary Fig. S17), 20 minute recordings starting from one minute before the first seizure following 4-AP injection were selected. Seizures with concurrent high-amplitude depolarizations such as SDs were excluded from analysis. 20 min recordings were filtered in two bands: DC-coupled (lowpass filter: <0.1 Hz) and seizure band (bandpass second order filter: 4-12 Hz). Signals were downsampled to 96 Hz. The RMS value of the seizure band was calculated with a 0.5 s sliding window and used to determine seizure onset and end. Epochs around -5 s to 2s relative to seizure start of the DC-coupled signal were extracted for analysing the DC-shifts. Zero voltage was set to the mean of the first 2s of the epoch and the maximum amplitude of the -5s to 0s period was then extracted and used as the amplitude of the pre-seizure DC-shift.

Current source density analysis applied to the low-frequency part of the potential (LFP), was calculated with the python open source Elephant library (Elephant electrophysiology analysis toolkit) using the class "Current Source Density analysis (CSD)" and the method 1D – StandardCSD was chosen for the linear gDNP array. A homogeneous conductivity of the neural tissue of σ=0.3 S/m across the different layers was used for the calculations.

The infraslow oscillation concurrency with the SWD shown in Fig. 4h was evaluated by performing the Hilbert transform to extract the phase of the DC-coupled signal (0.01-0.1 Hz) and associating it with the RMS between 5-9 Hz evaluated with an sliding window of 0.5s (typical bandwidth for the SWD). Supplementary Fig. S16 shows in more detail the dependency of ISO phase and SWD amplitude. The data shown in Fig. 4h illustrate the joint density probability indicating higher probability of a given RMS amplitude to ISO phase pair.

Chronic biocompatibility study

Device manufacture and sterilization. Two types of flexible gDNP where fabricated for the immunohistochemical study: One with graphene and one without graphene following the fabrication steps described above section (*Fabrication of gDNPs*). In the devices gDNP without graphene the graphene instead of being defined by RIE, was etched away. By doing so, we make sure that all the fabrication steps are equal for both, gDNP with and gDNP without graphene. For comparison to rigid devices currently available on the market, iridium Neuronexus electrodes (A1x32-Poly2-5mm-50s-177) with a thickness of 15µm and length 5mm were implanted. Devices were sterilised individually with ethylene oxide, using an Anprolene AN-74i sterilizer, performed according to manufacturer's instructions.

Surgical implantation of devices. Adult male Sprague-Dawley rats (230-280g) were used for this study (Charles River, England). All animals were kept in individually ventilated cages (Techniplast, GR1800) in groups of 3-4, housed at a constant ambient temperature of 21 ± 2°C and humidity of 40–50%, on a 12-h light, 12-h dark cycle. All rats were given free access to diet and water. Experimental procedures were conducted in compliance with the Animal welfare act 1998, with approval of the Home Office and local animal welfare ethical review body (AWERB). Animals were anaesthetized with Isoflurane (2-3%) throughout surgery, and depth of anaesthesia was monitored with the toe pinch reflex test. Animals were fixed to a stereotaxic frame (Kopf, model 900LS), and body temperature was maintained with a thermal blanket. A small craniotomy (~3mm) was made with a micro drill (WPI, OmniDrill35) above the somatosensory cortex, the dura was excised and one of three depth probe devices were implanted; i) graphene device, ii) no graphene device, or iii) Neuronexus device, at coordinates relative to bregma; anteroposterior (AP): 0mm, dorsoventral (DV): +3.5mm, and mediolateral: -1.5mm. The craniotomy site was sealed with Kwik Sil (WPI), secured with dental cement, the skin was sutured closed, and anaesthetic was withdrawn, with saline (20ml/kg) and buprenorphine (0.03mg/kg in saline) given subcutaneously to replace lost fluids and reduce post-operative pain.

Tissue collection and processing. Animals were culled at 2, 6 or 12 weeks' post-implantation dependent on the analysis to performed. Tissue was taken either for immunohistochemical analysis of cells related to inflammatory processes, or for cytokine analysis of inflammatory markers. For a further description of the techniques used, and analysis see Supplementary Information.

Histology. Animals were perfused with 4% PFA to fix tissue. Axial plane brain sections were cut at 50µm thickness with a vibrotome (Leica, VT1200). Sections at an approximate electrode site depth of 0.8mm were selected for staining. Sections were stained free-floating for two markers; i) ionized calcium binding adaptor molecule 1 (Iba1) to quantify microglial population, or ii) Glial fibrillary acidic protein (GFAP) staining to assess astrocyte presence (see Supplementary Methods for details of immunohistochemistry). Slides were imaged with a Leica SP8 confocal microscope with a 10x objective lens. Laser power and digital gain was kept consistent across imaging sessions. A single optical section of the tissue surrounding the probe sight was taken within the middle portion of the section as to avoid edge effects. Details of the analysis of histology is provided in Supplementary Methods section, Fig. S19- Fig. S20.

Enzyme-Linked ImmunoSorbent Assay (ELISA) Protocol. For ELISA, animals were culled by rising concentration of CO_2. Brain tissue was extracted, snap frozen in liquid nitrogen, and stored at -80 °C until further use. Brain tissue was lysed by addition of NP-40 lysis buffer (150 mM NaCl, 50 mM Tric-Cl, 1% Nonidet P40 substitute, Fluka, pH adjusted to 7.4) containing protease and phosphatase inhibitor (Halt™ Protease and Phosphatase Inhibitor Cocktail, ThermoFisher Scientific) followed by mechanical disruption of the tissue (TissueLyser LT, Qiagen). Samples were centrifuged at 5000RPM for 10 minutes, and the supernatant stored at 4 °C until further use. A bead-based multiplex ELISA kit was run, which included markers interleukin-1a (IL-1a), interleukin-1beta (IL-1b), interleukin-17 alpha (IL-17a), and interleukin-33 (IL-33) (Cat. No. 740401, Biolegend). The standard instructions for the kit were used, with protein loaded at a fixed volume of 15 µL. After incubation, beads were run on the BD FACSVerse flow cytometer, and the data analysed using LEGENDplexTM Data Analysis software.

Statistical analysis. For histological staining, all data sets are n=3, with the exception of 2-week graphene, which is n=4, and 12 weeks Neuronexus probes which are n=2, due to an inability to locate the probe location in histological sections for one animal implanted. For ELISA testing, gDNP with and without graphene hemisphere data sets are n=3 or 4 at all timepoints, while contralateral hemispheres were combined, giving n=7.

References

1. Perucca, P., Dubeau, F. & Gotman, J. Intracranial electroencephalographic seizure-onset patterns: effect of underlying pathology. *Brain* **137,** 183–196 (2014).

2. Modur, P. N. High frequency oscillations and infraslow activity in epilepsy. *Ann. Indian Acad. Neurol.* **17,** (2014).

3. Revankar, G. S. *et al.* Spreading depolarizations and seizures in clinical subdural electrocorticographic recordings. *Curr.*

Clin. Neurol. 77–90 (2017).

4. Dreier, J. P. The role of spreading depression, spreading depolarization and spreading ischemia in neurological disease. *Nature Medicine* **17,** 439–447 (2011).
5. Staba, R. J., Stead, M. & Worrell, G. A. Electrophysiological Biomarkers of Epilepsy. *Neurotherapeutics* **11,** 334–346 (2014).
6. Dell, K. L., Cook, M. J. & Maturana, M. I. Deep Brain Stimulation for Epilepsy: Biomarkers for Optimization. *Curr. Treat. Options Neurol.* **21,** 47 (2019).
7. Kuhlmann, L., Lehnertz, K., Richardson, M. P., Schelter, B. & Zaveri, H. P. Seizure prediction — ready for a new era. *Nat. Rev. Neurol.* **14,** 618–630 (2018).
8. Chari, A., Thornton, R. C., Tisdall, M. M. & Scott, R. C. Microelectrode recordings in human epilepsy: a case for clinical translation. *Brain Commun.* **2,** (2020).
9. Lee, S. *et al.* DC shifts, high frequency oscillations, ripples and fast ripples in relation to the seizure onset zone. *Seizure* **77,** 52–58 (2020).
10. Li, C. *et al.* Evaluation of microelectrode materials for direct-current electrocorticography. *J. Neural Eng.* **13,** 16008 (2015).
11. Hartings, J. A. How slow can you go? *Nat. Mater.* **18,** 194–196 (2019).
12. Major, S., Gajovic-eichelmann, N., Woitzik, J. & Jens, P. Oxygen- and pH-induced direct current (DC) artifacts on invasive platinum electrodes for electrocorticography. *Neurocrit. Care* 1–32 (2021). doi:In press
13. Khodagholy, D. *et al.* In vivo recordings of brain activity using organic transistors. *Nat. Commun.* **4,** 1575 (2013).
14. Kostarelos, K., Vincent, M., Hebert, C. & Garrido, J. a. Graphene in the Design and Engineering of Next-Generation Neural Interfaces. *Adv. Mater.* **29,** 1–7 (2017).
15. Blaschke, B. M. *et al.* Mapping brain activity with flexible graphene micro-transistors. *2D Mater.* **4,** (2017).
16. Hébert, C. *et al.* Flexible Graphene Solution-Gated Field-Effect Transistors: Efficient Transducers for Micro-Electrocorticography. *Adv. Funct. Mater.* **1703976,** 1703976 (2017).
17. Masvidal-Codina, E. *et al.* High-resolution mapping of infraslow cortical brain activity enabled by graphene microtransistors. *Nat. Mater.* **18,** 280–288 (2019).
18. Weltman, A., Yoo, J. & Meng, E. Flexible, penetrating brain probes enabled by advances in polymer microfabrication. *Micromachines* **7,** (2016).
19. Tien, L. W. *et al.* Silk as a multifunctional biomaterial substrate for reduced glial scarring around brain-penetrating electrodes. *Adv. Funct. Mater.* **23,** 3185–3193 (2013).
20. Coenen, A. M. L. & Van Luijtelaar, E. L. J. M. Genetic Animal Models for Absence Epilepsy: A Review of the WAG/Rij

Strain of Rats. *Behavior Genetics* **33,** 635–655 (2003).

21. Terlau, J. *et al.* Spike-wave discharges in absence epilepsy: segregation of electrographic components reveals distinct pathways of seizure activity. *J. Physiol.* (2020). doi:10.1113/JP279483
22. Zijlmans, M. *et al.* High-frequency oscillations as a new biomarker in epilepsy. *Ann. Neurol.* **71,** 169–78 (2012).
23. Jacobs, J. *et al.* High-frequency oscillations (HFOs) in clinical epilepsy. *Progress in Neurobiology* **98,** 302–315 (2012).
24. Ikeda, A. *et al.* Focal ictal direct current shifts in human epilepsy as studied by subdural and scalp recording. *Brain* **122,** 827–838 (1999).
25. Wu, S. *et al.* Role of ictal baseline shifts and ictal high-frequency oscillations in stereo-electroencephalography analysis of mesial temporal lobe seizures. *Epilepsia* **55,** 690–698 (2014).
26. Vanhatalo, S. *et al.* Very slow eeg responses lateralize temporal lobe seizures: An evaluation of non-invasive DC-EEG. *Neurology* **60,** 1098–1104 (2003).
27. Duan, X. *et al.* Intracellular recordings of action potentials by an extracellular nanoscale field-effect transistor. *Nat. Nanotechnol.* **7,** 174–179 (2012).
28. Hess, L. H. Graphene Transistors for Biosensing and Bioelectronics. *Proc. IEEE* **101,** 1780–1792 (2013).
29. Hess, L. H. *et al.* High-transconductance graphene solution-gated field effect transistors. *Appl. Phys. Lett.* **99,** (2011).
30. Garcia-Cortadella, R. *et al.* Distortion-Free Sensing of Neural Activity Using Graphene Transistors. *Small* **16,** (2020).
31. Lecomte, A. *et al.* Silk and PEG as means to stiffen a parylene probe for insertion in the brain: Toward a double time-scale tool for local drug delivery. *J. Micromechanics Microengineering* **25,** (2015).
32. Fueta, Y. & Avoli, M. Effects of antiepileptic drugs on 4-aminopyridine-induced epileptiform activity in young and adult rat hippocampus. *Epilepsy Res.* **12,** 207–215 (1992).
33. Padmanabhan, K. & Urban, N. N. Disrupting information coding via block of 4-AP-sensitive potassium channels. *J. Neurophysiol.* **112,** 1054–1066 (2014).
34. Zakharov, A., Chernova, K., Burkhanova, G., Holmes, G. L. & Khazipov, R. Segregation of seizures and spreading depolarization across cortical layers. *Epilepsia* **60,** 2386–2397 (2019).
35. Hartings, J. A. *et al.* Direct current electrocorticography for clinical neuromonitoring of spreading depolarizations. *J. Cereb. Blood Flow Metab.* **37,** 1857–1870 (2017).
36. Harriott, A. M., Takizawa, T., Chung, D. Y. & Chen, S. P. Spreading depression as a preclinical model of migraine. *Journal of Headache and Pain* **20,** (2019).
37. Buzsáki, G. & Silva, F. L. da. High frequency oscillations in the intact brain. *Progress in Neurobiology* **98,** 241–249 (2012).
38. Chaudhary, U. J. *et al.* Mapping preictal and ictal haemodynamic networks using video- electroencephalography and

functional imaging. *Brain* **135,** 3645–3663 (2012).

39. Ikeda, A. *et al.* Active direct current (DC) shifts and 'Red slow': two new concepts for seizure mechanisms and identification of the epileptogenic zone. *Neuroscience Research* **156,** 95–101 (2020).
40. Kamarajan, C., Pandey, A. K., Chorlian, D. B. & Porjesz, B. The use of current source density as electrophysiological correlates in neuropsychiatric disorders: A review of human studies. *Int. J. Psychophysiol.* **97,** 310–322 (2015).
41. Flynn, S. P., Barrier, S., Scott, R. C., Lenck-Santini, P. P. & Holmes, G. L. Status epilepticus induced spontaneous dentate gyrus spikes: In vivo current source density analysis. *PLoS One* **10,** (2015).
42. Coenen, A. M. L. & Van Luijtelaar, E. L. J. M. The WAG/Rij rat model for absence epilepsy: age and sex factors. *Epilepsy Res.* **1,** 297–301 (1987).
43. Orlowska-Feuer, P. *et al.* Infra-slow modulation of fast beta/gamma oscillations in the mouse visual system. *J. Physiol.* **599,** 1631–1650 (2021).
44. Garcia-Cortadella, R. *et al.* Graphene active sensor arrays for long-term and wireless mapping of wide frequency band epicortical brain activity. *Nat. Commun.* **12,** (2021).
45. Bahari, F. *et al.* Spreading Depression and Seizure Unification Experimentally Observed in Epilepsy. *bioRxiv* **2,** (2018).
46. Dreier, J. P. *et al.* Spreading convulsions, spreading depolarization and epileptogenesis in human cerebral cortex. *Brain* **135,** 259–275 (2012).
47. Dreier, J. P. & Reiffurth, C. Exploitation of the spreading depolarization-induced cytotoxic edema for high-resolution, 3D mapping of its heterogeneous propagation paths. *Proceedings of the National Academy of Sciences of the United States of America* **114,** 2112–2114 (2017).
48. De Tisi, J. *et al.* The long-term outcome of adult epilepsy surgery, patterns of seizure remission, and relapse: A cohort study. *Lancet* **378,** 1388–1395 (2011).
49. Kanazawa, K. *et al.* Intracranially recorded ictal direct current shifts may precede high frequency oscillations in human epilepsy. *Clin. Neurophysiol.* **126,** 47–59 (2015).
50. Lauritzen, M. *et al.* Clinical relevance of cortical spreading depression in neurological disorders: Migraine, malignant stroke, subarachnoid and intracranial hemorrhage, and traumatic brain injury. *Journal of Cerebral Blood Flow and Metabolism* **31,** 17–35 (2011).
51. Zhang, B. *et al.* Low-temperature chemical vapor deposition growth of graphene from toluene on electropolished copper foils. *ACS Nano* **6,** 2471–2476 (2012).
52. Schaefer, N. *et al.* Improved metal-graphene contacts for low-noise, high-density microtransistor arrays for neural sensing. *Carbon N. Y.* **161,** 647–655 (2020).

53. Jin, H. J. *et al.* Water-stable silk films with reduced β-sheet content. *Adv. Funct. Mater.* **15,** 1241–1247 (2005).

54. Rockwood, D. N. *et al.* Materials fabrication from Bombyx mori silk fibroin. *Nat. Protoc.* **6,** 1612–31 (2011).

55. Vepari, C. & Kaplan, D. L. Silk as a biomaterial. *Prog. Polym. Sci.* **32,** 991–1007 (2007).

56. Cao, Y. & Wang, B. Biodegradation of silk biomaterials. *Int. J. Mol. Sci.* **10,** 1514–1524 (2009).

57. Gobin, A. S., Froude, V. E. & Mathur, A. B. Structural and mechanical characteristics of silk fibroin and chitosan blend scaffolds for tissue regeneration. *J. Biomed. Mater. Res. - Part A* **74,** 465–473 (2005).

58. Russo, E. *et al.* Upholding WAG/Rij rats as a model of absence epileptogenesis: Hidden mechanisms and a new theory on seizure development. *Neuroscience and Biobehavioral Reviews* **71,** 388–408 (2016).

59. van Luijtelaar, G. & van Oijen, G. Establishing Drug Effects on Electrocorticographic Activity in a Genetic Absence Epilepsy Model: Advances and Pitfalls. *Frontiers in Pharmacology* **11,** (2020).

Acknowledgments

Funding: This work has received funding from the European Union's Horizon 2020 research and innovation programme under Grant Agreement No 881603 (GrapheneCore3). The ICN2 is supported by the Severo Ochoa Centres of Excellence programme, funded by the Spanish Research Agency (AEI, grant no. SEV-2017-0706), and by the CERCA Programme / Generalitat de Catalunya. A.B.C. is supported by the International PhD Programme La Caixa - Severo Ochoa (Programa Internacional de Becas "la Caixa"-Severo Ochoa). This work has made use of the Spanish ICTS Network MICRONANOFABS partially supported by MICINN and the ICTS 'NANBIOSIS', more specifically by the Micro-NanoTechnology Unit of the CIBER in Bioengineering, Biomaterials and Nanomedicine (CIBER-BBN) at the IMB-CNM. We also acknowledge funding from Generalitat de Catalunya (2017 SGR 1426), and the 2DTecBio project (FIS2017-85787-R) funded by the "Ministerio de Ciencia, Innovación y Universidades" of Spain, the "Agencia Estatal de Investigación (AEI)" and the "Fondo Europeo de Desarrollo Regional (FEDER/UE)". Part of this work is co-funded by the European Regional Development Funds (ERDF) allocated to the Programa operatiu FEDER de Catalunya 2014-2020, with the support of the Secretaria d'Universitats i Recerca of the Departament d'Empresa i Coneixement of the Generalitat de Catalunya for emerging technology clusters devoted to the valorization and transfer of research results (GraphCAT 001-P-001702)"

A.B.C. acknowledges that this work has been done in the framework of the PhD in Electrical and Telecommunication Engineering at the Universitat Autònoma de Barcelona.

R.W. is funded by a Senior Research Fellowship awarded by the Worshipful Company of Pewterers.

D. R. is a Biotechnology and Biological Sciences Research Council (BBSRC) LIDo sponsored PhD student. The authors would like to thank Prof. Matthew Walker and Prof. Louis Lemieux (UCL Queen Square Institute of Neurology) for their comments on the manuscript.

Author contributions: A.B.C. carried out most of the fabrication and characterization of the gDNPs, contributed to the design and performance of the in vivo experiments, analysed the data and wrote the manuscript. E.M.C. contributed to the design and planning of the in vivo experiments and support to the DC-shift and SD analysis of the in vivo data. R.W., T.M.S. performed the in vivo experiments. D.R., contributed to the in vivo experiments and DC-coupled recordings with the glass micropipette. N.S., E.R.L., X.I. and J.M.D.C. contributed to the fabrication and characterization of the gDNPs. E.D.C., J.B. and C.H., contributed to the growth, transfer and characterisation of CVD graphene used in the gDNPs. E.P.A., A.H. and E.R.L., contributed to the optimisation of the silk-fibroin stiffening protocol of the gDNPs. J.M.A., contributed to the fabrication of the custom electronic instrumentation and development of a Python-based user interface. D.V. contributed to the python scripts and technical discussions. J.R.S. reviewed the manuscript. J.F. and J.S. contributed to the mechanical assessment of the silk-fibroin and the silk-fibroin back-coated gDNPs. M.D. performed all surgeries for the biocompatibility study. A.D. and K.B. contributed to the capture of histological images and image-processing and analysis. S.S and K.B contributed to the preparation and review of the manuscript. A.G.B. contributed in the design and fabrication of the custom electronic instrumentation, development of a custom gSGFET Python library and analysis of the data.

R.V., K.K., R.W., A.G.B., and J.A.G. participated in the design of all experiments and thoroughly reviewed the manuscript. All authors read and reviewed the manuscript.

Competing interests: C.G. is the owner of g.tec medical engineering GmbH and Guger Technologies OG.

Data and materials availability: Data from gDNP characterization, biocompatibility assessment will be shared upon request to the corresponding authors, after agreement on the files format. Data from electrophysiological recordings are openly available in [repository name] at http://doi.org/[doi], reference number [xxxxx].